Advances in Science and Technology Research Journal

Advances in Science and Technology Research Journal, 2027, 21(1), 287–301
https://doi.org/10.12913/22998624/235787
ISSN 2299-8624, License CC-BY 4.0

Received: 2026.06.28
Accepted: 2026.11.15
Published: 2026.12.01

Enhancing the microstructure, corrosion resistance, and bioactivity of biodegradable Zn–1Mg alloys through Mn addition

Fatima Diaa Wahabn[1*], Nawal Mohammed Dawood[1*], Ayad Mohammed Nattah[1]

[1] College of Materials Engineering, University of Babylon, Iraq
* Corresponding author's e-mail: mat.newal.mohammed@uobabylon.edu.iq

ABSTRACT

Because of their superior mechanical, biodegradable, and biocompatible qualities, zinc-based alloys have drawn greater attention to biodegradable metals. In this study, manganese was added to a Zn-1Mg alloy at different levels (0.2, 0.3, and 0.4 wt.%). The alloys were prepared via the powder metallurgy technique. The chemical composition, phase distribution, and microstructural characteristics of the Zn-1Mg alloys were evaluated before and after Mn addition. Additionally, the corrosion behavior of the alloys was investigated in Hank's solution, and their Vickers microhardness was measured. Furthermore, biological performance evaluations, including contact angle and bioactivity tests, were conducted to assess the suitability of these alloys for implant applications. Overall, the study demonstrated that varying amounts of Mn addition hold significant potential for improving the hardness, corrosion resistance, and biological properties of Zn-1Mg alloys. Through metallographic observation Light Optical microscope (LOM), X-ray diffraction (XRD), and Scanning electron microscopy (SEM) analysis of the alloy, it was found that Mn addition to Zn-1Mg alloy resulted in the formation of the α-Zn matrix and Mg2Zn11 phase. The B3 alloy exhibited the highest hardness of 86.21 HV, compared with 66.09 HV for the base alloy. The maximum compressive strength was recorded for the B3 alloy, reaching 115 MPa. Mn addition, improved corrosion resistance, reducing the corrosion rate to 0.099 mm/y for the B2 alloy, corresponding to an improvement of 87.126%, the contact angle decreased after Mn addition, indicating improved surface wettability. The outcomes showed that the addition of Mn significantly improved the bioactivity behavior of the samples under study. SEM images after immersion revealed a greater formation of HA particles on the surfaces of the Mn-added alloys compared with the base alloy. Different Mn contents were found to be optimal for different properties; 0.3 wt.% Mn provided the best corrosion resistance, whereas 0.4 wt.% Mn exhibited the highest hardness, compressive strength, and surface wettability.

Keywords: powder metallurgy, Zn-1Mg-based bio-alloy, microstructure, mechanical properties, electrochemical behavior, bioactivity and contact angle test.

INTRODUCTION

Medical technology and biomaterials developments have generated significant interest over the last 4 decades due to their ability to enhance human life through the replacement as well as repair of hard and soft tissues, including blood vessels, bone, cartilage, and even complete organs [1]. Biomaterials are an inert material, synthetic or natural, that are developed to re-place a specific portion of a system or a certain physiological function [2]. More research was done on degradable metal materials. The study focused on three main types of biodegradable metals: magnesium-based, zinc-based, and iron-based [3]. Every part of the body needs zinc for proper health; bone and muscle contain about 85% of the mineral. It participates in numerous enzymatic reactions and is an essential component of the structure of macromolecules and enzymes

[4]. The electrode potential of zinc (−0.762 V) is between that of iron (−0.444 V) and magnesium (−2.372 V), indicating its high chemical activity [1]. One major disadvantage of pure zinc is its low strength (σUTS ~ 30 MPa) and plasticity (ε < 0.25%), which makes it unsuitable for most medical applications as a possible biodegradable structural support [5]. However, used as bioresorbable implants, zinc-based BMs may also come into certain problems. The primary barrier preventing the clinical use of biodegradable Zn-based BMs is their non-uniform break-down behavior, which is the most severe issue. This degrading behavior results from the addition of alloying elements (Mg, Sr, Ca, etc.) because pure zinc does not meet the mechanical property requirements for implants. Localized corrosion comes from the necessary formation of galvanic cells caused by the segregation of these alloying elements. Furthermore, galvanic corrosion results in severe localized corrosion once micro-galvanic interaction between the Zn matrix and precipitated phase starts [6]. Magnesium, manganese, calcium, strontium, iron, lithium, and other elements that are often necessary for human health are among the few alloying elements that can be chosen [7]. The best biomaterials to produce biodegradable devices are those based on magnesium and zinc. The use of magnesium-based biomaterials in biological applications has been restricted due to their rapid disintegration and excessive production of degradation products [8]. Since adding Mg to Zn has been shown to greatly improve corrosion resistance and mechanical properties, Zn-Mg alloys are the most commonly used in medical applications [9]. Because of its biocompatibility and capacity to produce reinforcing secondary phases, magnesium is especially beneficial. In Zn-Mg systems, Mg2Zn11 precipitates contribute to hardening via dispersion effects [10]. In biomedical applications, controlling corrosion rates is just as important as enhancing mechanical performance when creating Zn-Mg alloys for controlled deterioration [11]. For the purpose of evaluating the mechanical properties of Zn-Mg alloys, the addition of strategic alloying elements, such as Mn, has been carefully studied [12]. The underlying mechanisms are influenced by a gradual loss of mass. In 2024, Lu et al. [15] manufactured a Zn-0.8Mg-0.2Mn alloy with a 26% elongation and a tensile strength of 414 MPa. Grain boundary strengthening, precipitation strengthening, and second-phase strengthening all contribute to the strength of the as-extruded zinc alloy. With extended immersion, the degradation of Zn alloy in Hank's solution showed a decreasing pattern until stabilizing at 16 μm/year. After varying immersion times, the Zn alloy's tensile strength was largely similar, although there was a noticeable reduction in elongation. In 2025, Cheng et al. [20] studied the effects of varying manganese concentrations (0.1, 0.3, 0.5, and 0.8 weight percent) on the characteristics of pure zinc. The results demonstrated that zinc-manganese alloys were primarily composed of a zinc matrix and a MnZn13 phase, which resulted in a significant improvement of the mechanical properties with Vickers hardness of 78 HV, ultimate tensile strength (UTS), yield strength (YS), and elongation up to 117.3 MPa, 110.4 MPa, and 14%, respectively. The purpose of this study was to methodically investigate the impacts of minor manganese additions (0.2, 0.3, and 0.4 wt.%) on the Zn–1Mg biodegradable alloy. All alloys were fabricated via the powder metallurgy route. The influence of Mn additions on the microstructure, Vickers micro hardness, and electrochemical corrosion resistance was comprehensively evaluated. Furthermore, contact angle measurements and in vitro bioactivity tests in Hank's solution were performed to assess the surface wettability and bone-bonding ability, clarifying the role of Mn in optimizing the performance of Zn-1Mg alloys for potential biomedical implant applications.

EXPERIMENTAL PROCEDURES

Materials and methods

Pure zinc powder (99.9%, particle size (25 μm, Xian Function Material Group CO., LTD. P.R. China), pure magnesium (99.9%, particle size 28 μm, Xian Function Material Group CO., LTD. P.R. China) and pure manganese (99.5%, particle size (24 μm, Qingdao Hesiway Industrial Co., Ltd. China) were used for the preparation of Zn-1Mg and Zn-1Mg-xMn (x= 0.2, 0.3 and 0.4 wt.%) by powder technology. All powders were weighed with an accuracy of ±0.0001 g using a sensitive digital balance type (L220S-D) from Germany. The main alloy system is Zn-1Mg, in which zinc and magnesium represent the major constituents, while manganese was added as an alloying element, consisting of the following weight percentages: 99 wt.% Zn, 1 wt.% Mg and (0.2, 0.3, 0.4) wt.% Mn.

After weighing, a planetary ball mill kind (Bench-Top Planetary Automatic Ball Mill, MTI Corporation) was used for the wet mixing (Exactly 0.5 cc of ethyl alcohol was used to minimize the temperature generated by friction between the balls and the mill walls and powders). Seven different-sized stainless-steel balls were used for five hours to ensure a uniform and even dispersion of powder particles. The Zn-1Mg powder mixture was then milled using planetary ball milling ma-chine with ball to powder ratio of 10:1 according to at 350 rpm for 5 hours. After that, they were placed in polyethylene zip-lock bags. Later, the mixed powder was pressed by an American electric- hydraulic press one channel device (model number CT340-CT440) at 700 MPa using a cylindrical stainless-steel die of 13 mm diameter. The sintering process was performed under Ar protective atmosphere (99.95%) to avoid oxidation. While sintering in a tube furnace type SRJX-2-13, the green compacts were heated from room temperature to 200 °C and were continued to be sintered at 550 °C for about two hours with a heating rate of 10 °C/min for both sintering stages. Figure 1 shows the heating cycle of the sintering process. Once sintering was completed, while maintaining the argon flow, the samples were left to cool slowly inside the furnace down to room temperature. Table 1 clarifies the code of samples after sintering.

Microstructure

The microstructure of the materials was studied using an optical microscope (BEL PHOTONICS) and a scanning electron microscope (SEM-type VEGA 3 SBU) equipped with an EDS analyzer (OXFORD Instruments AZtec). Prior to the observations, using Sic grinding sheets, the samples were ground (P180-P3000), to achieve a uniform surface. Then, they were polished with diamond paste D2 (UR-diamant, 3.1 μm) and finally polished on suspension Etosil E (Metalco, 0.25 μm). After a distilled water wash, the samples were dried. The etchant used to show microstructural characteristics was a 4% nitric acid-alcohol mixture [10]. The phases present were identified using an XRD analysis. XRD machine (XRD 6000, Shimadzo, Japan). It was performed on all samples, both before and after Mn addition, on Shimadzu XRD-6000 manufactured in Japan. The Cu target was measured at 30 mA and 40 kV, with a scanning speed of 5 degrees per minute over 30 to 80 degrees.

Mechanical test

Hardness measurement

Micro-hardness property testing of as-sintered samples was performed using ASTM-E384-17 standard type (Digital Micro hardness tested HV-1000) at a load of 100 g for 10 s, as reported by [21, 22]. The hardness of each sample was determined by averaging the values from five indents.

Table 1. Clarify the code of the samples

No.	Alloy code.	Chemical composition (wt.%).
1	A	Zn-1Mg base alloy
2	B1	Zn-1Mg+0.2% Mn
3	B2	Zn-1Mg+0.3% Mn
4	B3	Zn-1Mg+0.4% Mn

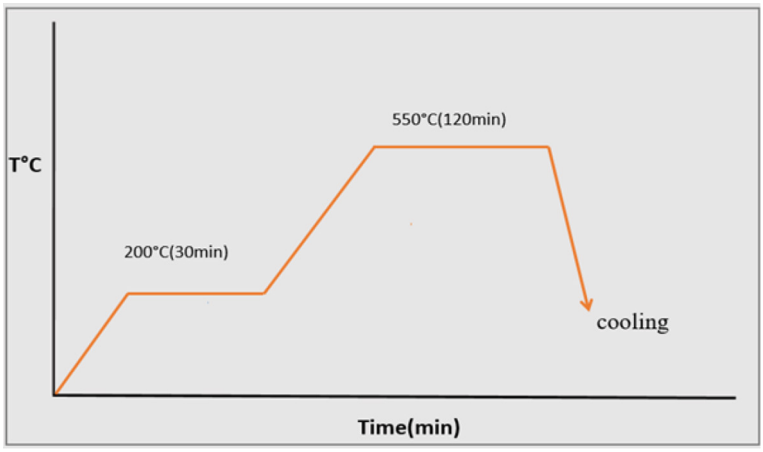


Figure 1. The heating cycle of the sintering process

Compression test

Compression testing was performed using via computer control electronic general testing machine,, model WDW-200, No. W1124), as per the ASTM B925-08 specification,with dimension of length (l) to diameter (d) ratio of 2, i.e L/d= 2.The rate of loading speed was 0.2 mm/min.

Electrochemical behavior

After polishing, assessment of the electrochemical behavior was carried out in the form of the open circuit potential (OCP) measurements and potentiodynamic polarization (PDT) analysis. The tests were performed using a Bio-Logic SP-200 potentiostat (BioLogic Science Instruments, Seyssinet-Pariset, France), equipped with EC-Lab software V11.18. Saturated calomel (SCE) was used as the reference electrode, platinum worked as an auxiliary electrode, and the tested alloy was provided as the working electrode in this three-electrode electrochemical cell. Every electrochemical test analysis was performed at 37 ± 1°C (pH= 7.2) in Hank's solution. Until a consistent potential was reached, the OCP measurements were shown for about 80 minutes. Subsequently, the PDT scans were performed. The PDT curves were measured from − 250 mV to +250 mV relative to the OCP at a scan rate of 0.333 mV/s. The following formula was used to determine the corrosion rate (CR) of the specimens [23–25]:

$$CR = K \cdot \frac{icorr \cdot EW}{\rho} \quad (1)$$

where: K, conversion factor (3.27×10^{-3} (mm/g)/(μA/cm·year), EW – is the dimensionless equivalent weight of alloy, $icorr$ – corrosion current density (μA/cm^2), and ρ – density (g/cm^3) of the Zn-based alloys.

The equivalent weight (EW) and density (ρ) values used in the corrosion rate calculations according to ASTM G102 are listed in Table 2.

Table 2. The equivalent weight (EW) and density (ρ) values

Alloy	ρ(g/cm^3)	EW(g/eq)
A	4.84	32.131
B1	6.84	31.987
B2	7.29	32.135
B3	6.726	31.935

Bioactivity test

In vitro bioactivity tests were conducted by immersing the specimens in 50 mL of simulated body fluid (SBF) (pH = 7.4) at 37 ± 1 °C for 14 days [26]. After immersion, the specimens are removed from the fluid and dried at 40 °C for 1 h before the surface analysis. The specimens' apatite layer formation is identified, analyzed and confirmed using (SEM) and (XRD).

Contact angle test

The hydrophobicity or wettability for all specimens were determined using the droplet's contact angle (θ) on a solid surface used Hank's solution. A CCD camera was used to measure contact angle, and the contact angle measurement was taken immediately after the droplet was placed on the solid surface by a 1 µL pipettor. This device, located in Department of Ceramics, material Engineering, Babylon University, computes contact angles and determines their average values, providing a real-time data graph that tracks changes in contact angles while video is being recorded.

RESULTS AND DISCUSSION

XRD patterns for alloys

XRD investigation revealed significant differences in peak intensities across the alloys. XRD results showed that the hexagonal zinc phase (α-Zn) is the dominant phase in all alloys, exhibiting sharp, high-intensity peaks. Additionally, low peaks of the Mg_2Zn11 phases appeared in the Zn-1Mg alloy, which are considered an intermetallic phase. This indicates partial dissolution of magnesium in the zinc alloy. However, when manganese was added at 0.2–0.4 wt.%, the effect was limited at this percentage, as no clear peaks of Zn-Mn were observed. This suggests that manganese at this percentage is partially dissolved in the zinc crystal lattice as a solid solution or is present in such small quantities that it is barely detectable by the XRD technique [20]. Also, Figure (2 a, b, c and d) show that the formed phases were identified via XRD by comparison with standard reference patterns JCPDS cards numbers and this is similar to [19, 20, 23].

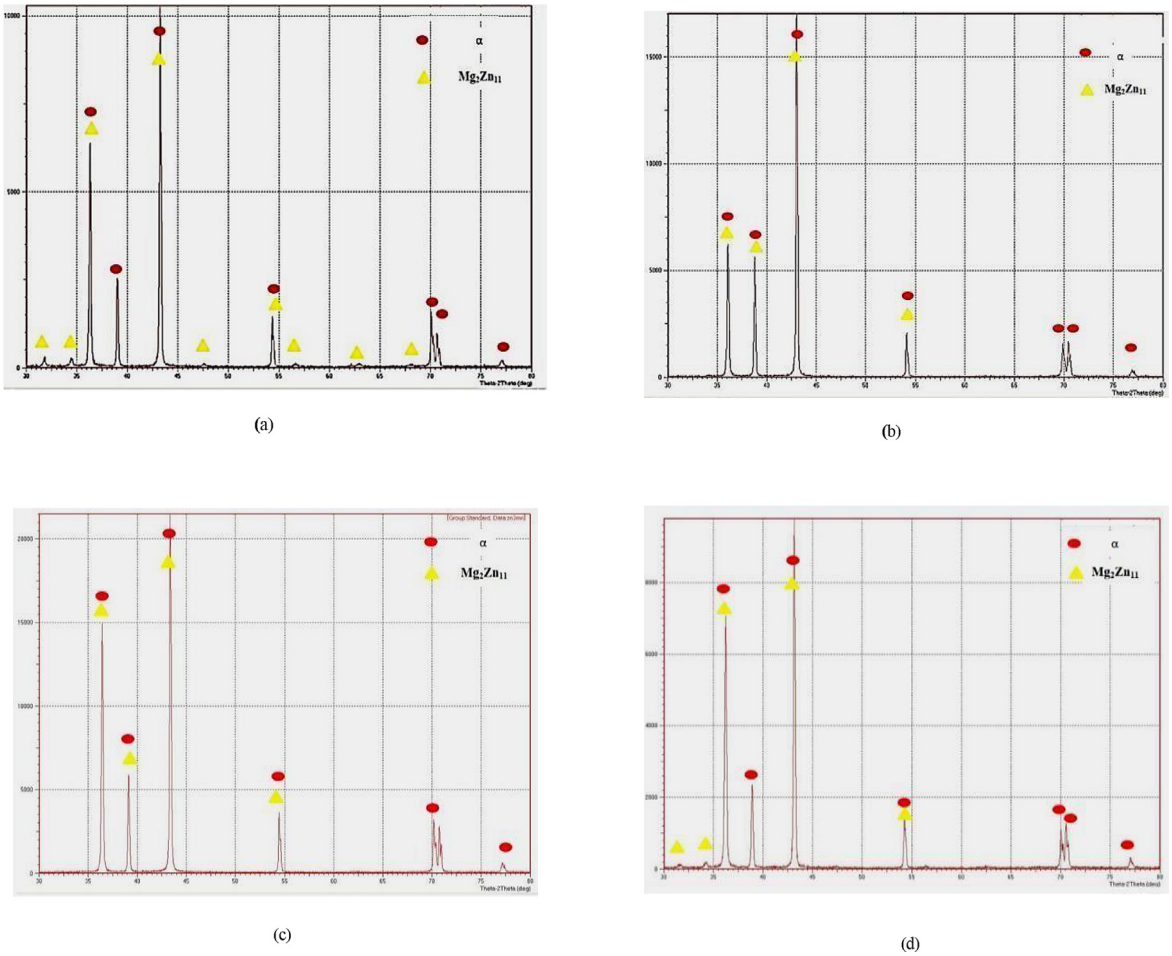


Figure 2. XRD patterns of (a) sample A, (b) sample B1, (c) sample B2, and (d) sample B3

Light optical microscope (LOM) analysis

Every property of the Zn-1Mg alloy significantly influenced by the microstructure. Figure 3(a, b, c and d) shows the metallographic structure of Zn-1Mg and Zn-1Mg-xMn alloys. It can be observed from Figure (3a-d) that Zn-1Mg-xMn alloys are mainly composed of a primary matrix and a secondary phase. The bright phase represents a solid solution of zinc, while the secondary

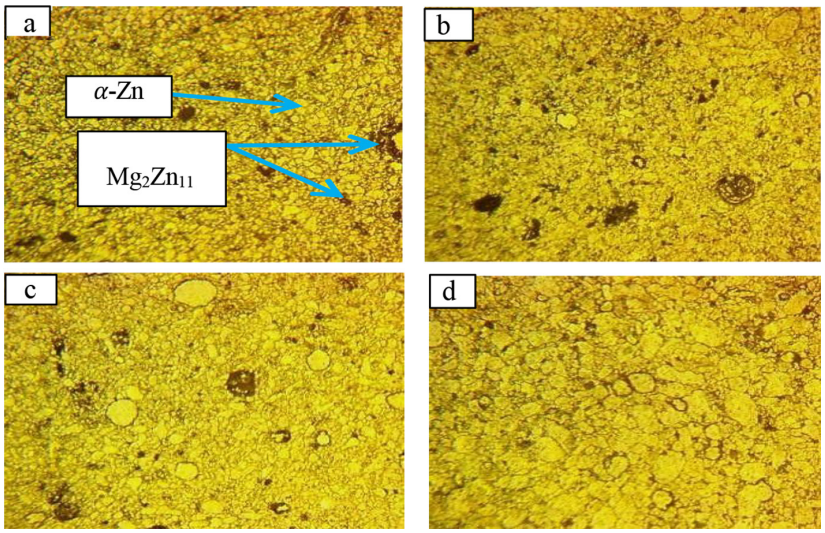


Figure 3. Optical micrographs of (a)Zn-1Mg, (b)Zn-1Mg+0.2Mn, (c)Zn-1Mg+0.3Mn, (d) Zn-1Mg+0.4Mn alloy

phase is composed of eutectic (α-Zn+Mg_2Zn_{11}). These result are similar to [11, 23]. In previous studies it was also shown [27, 28] that the Zn-0.8Mg alloys were hypoeutectic in their as-cast form, meaning they had a eutectic mixture of (α-Zn + Mg_2Zn_{11}) and primary Zn dendrites.

SEM and energy dispersive spectroscopy (EDS) analysis results

In SEM it was discovered that the base alloy (A), as displayed in Figure (4a-d), has a microstructure represented by the bright phase, which is a zinc-rich region as the alloy matrix, and the dark region represents eutectic (α-Zn+Mg_2Zn_{11}), while in samples B1, B2, and B3, the addition of manganese resulted in a microstructure nearly identical to that of the base alloy [24]. As can be observed in the SEM image in Figure 4, the increased Mn percentage caused an apparent increase in the amount of dark secondary phases, which are mainly distributed along the grain boundaries and are rich in Mg as well as Mn, thus promoting the formation of intermetallic phases within the zinc matrix. It is known that the results of the EDS test are usually close to the values [18, 20]. Because EDS analysis gives the values that do not cover the entire surface area of the samples. However, it gives an analysis

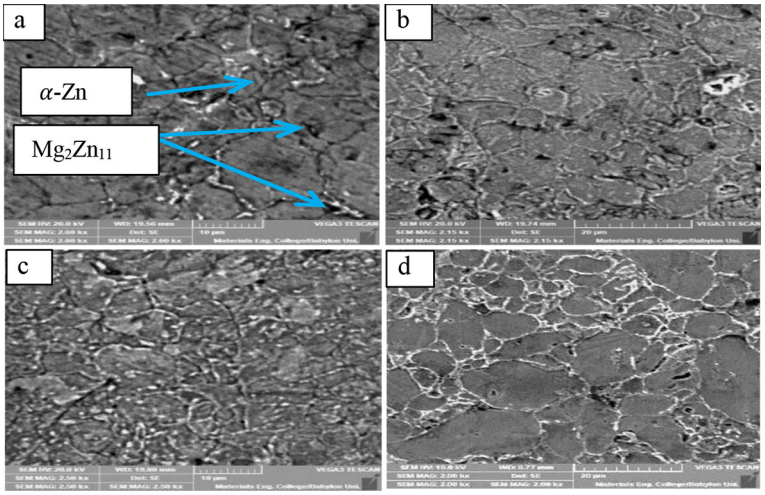


Figure 4. SEM microscopy of (a)Zn-1Mg, (b)Zn-1Mg+0.2Mn, (c) Zn-1Mg+0.3Mn, (d) Zn-1Mg+0.4Mn alloy

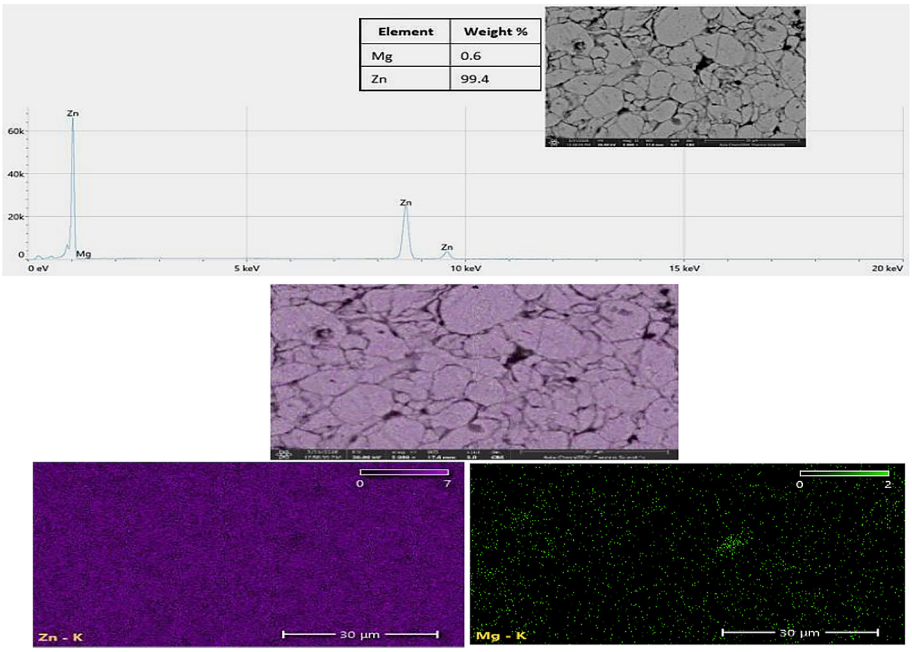


Figure 5. EDS of the sample (A)

of the place where the electron strike occurred. The EDS microanalysis results are shown in Figure 5 for base alloy, whereas Figures 6, 7 show B1 and B3, respectively, [23, 29]. Figures (5, 6, and 7) represent the EDS analysis of the base alloy Zn-1Mg and alloys B1 and B3 with Mn addition ratios of 0.2 wt.%, 0.4 wt.%, respectively. It is clear from the figure that there is a high percentage of Zn, reaching 83.3 wt.%, and Mg at a percentage of 0.5 wt.%. This is expected because the base alloy is Zn-1Mg. In the EDS analysis for samples B1 and B3, it is clear that there are both Zn and Mg in addition to Mn. This is due to the Mn addition to the alloy. The EDS analysis of alloy B3 shows that the manganese percentage has increased from 0.5 wt.% for alloy B1 to 0.9 wt.% for alloy B3 [23]. This is because the base alloy's Mn percentage raised while the Zn percentage lowered.

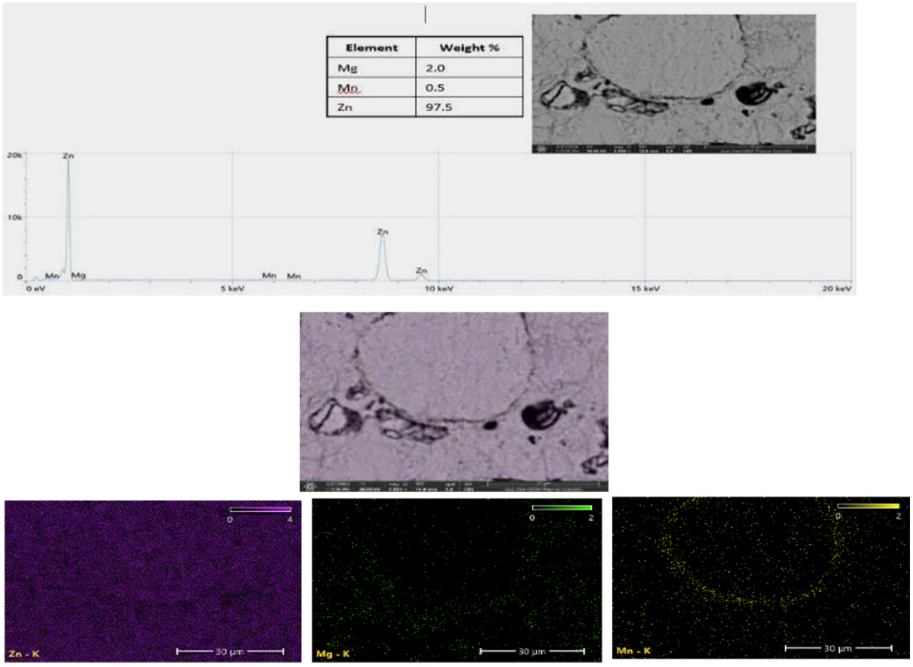


Figure 6. EDS of the sample (B1)

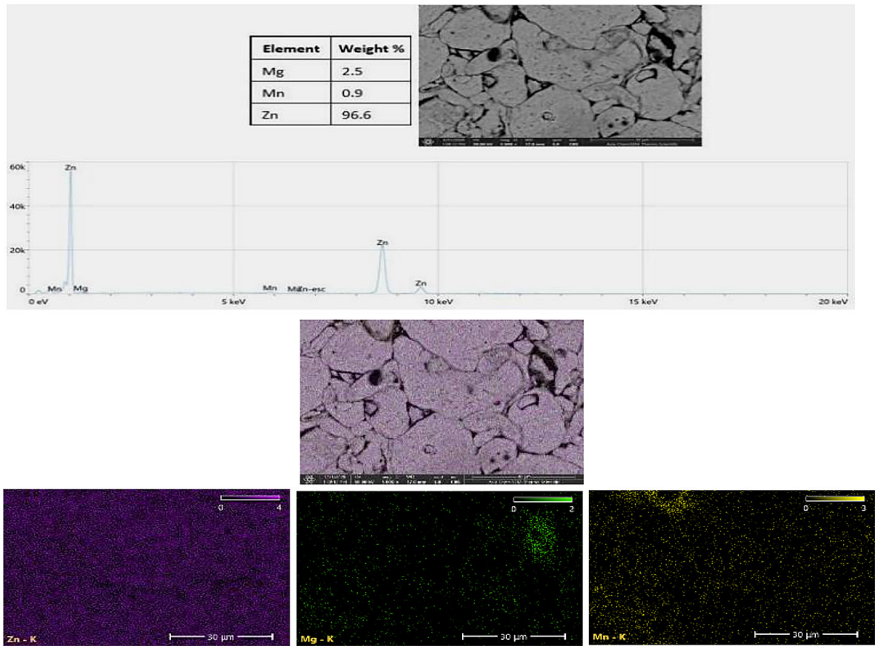


Figure 7. EDS of the sample (B3)

Mechanical properties

Hardness test

As shown in Figure 8 the hardness value of Zn-1Mg alloy increased further with the addition of Mn. The hardness of the base alloy (A) reached 66.09. It increased to 80.19 for alloy B1 when 0.2 wt.% Mn was added. However, increases in the hardness of sample B2 to 83.33 when adding 0.3 wt.% Mn, and to 86.21 for alloy B3 when adding 0.4 wt.% Mn were noticed. The results of the hardness test showed that increasing the percentage of Mn led to an increase in Vickers hardness, as shown in Figure 8, indicating that the more manganese is added, the higher the hardness of the alloy. The increase in hardness is related to the increase in the percentage of Mn, as Mn acts as a strengthening agent in the solid solution by distorting the crystal lattice and hindering the movement of dislocations. In addition, it contributes to the distribution of grains, reducing their size and increasing the number of grains [16]. It also leads to the formation of intermetallic phases within the substrate. Therefore, the hardness will improve according to the Hall-Petch relationship. This suggests that the strength and ductility of Zn-1Mg alloys are greatly enhanced by the addition of Mn. The second factor is second phase precipitates. Thus, the formation of the hard intermetallic phase of Mg2Zn11 can effectively block dislocation motion and strengthen the alloy as a result, a gradual increase in the percentage of Mn up to 0.4 wt.% will clearly enhance the hardness of the Zn-1Mg-xMn alloy [20, 23].

Compression test

The compressive strength of the alloy with (0.2, 0.3 and 0.4 wt.%) of manganese, where the addition of manganese led to an increase in the

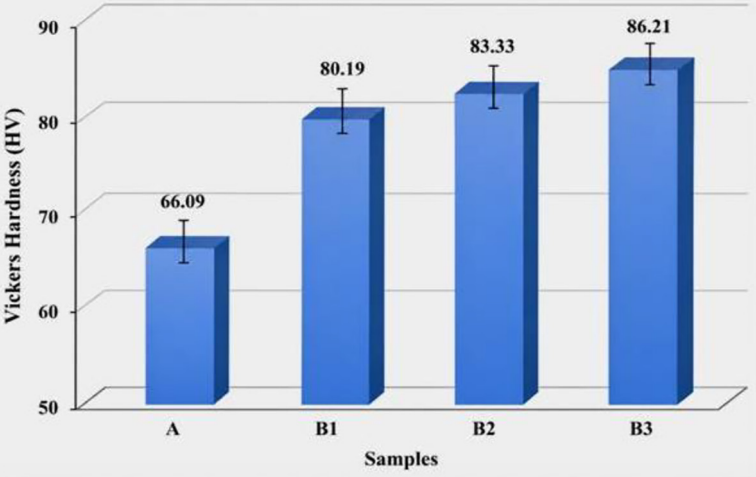


Figure 8. Effect of Mn percentage on the hardness of alloys A, B1, B2, and B3 alloy

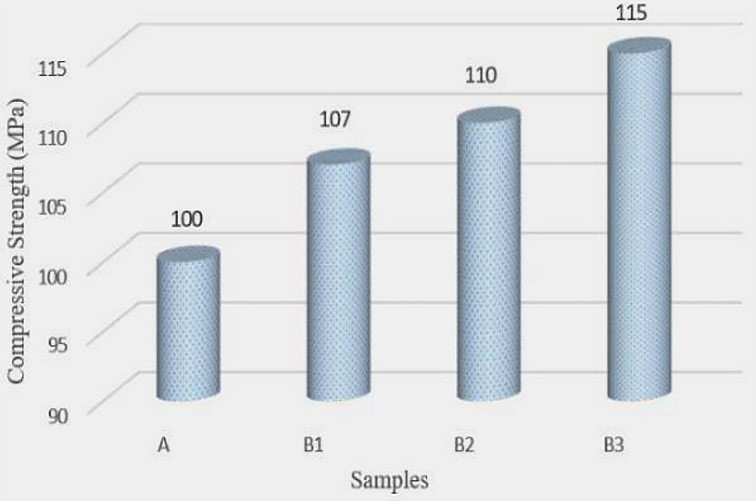


Figure 9. The compressive strengths of the A, B1, B2, B3 alloys

compressive strength of the alloy, as shown in Figure 9. The compressive strength depends on several factors, including the particle size and the composition of the alloys. The strengthening process can occur by changing the composition of the matrix alloy, which occurs through the addition of elements. The rate of grain size will be reduced by the presence of the strengthening addition, which works to impede grain growth, and this is due to the presence of manganese refining the grain size, which gives good mechanical properties [16, 30].

Electrochemical behavior

The OCP-time in Hank's solution was measured at 37 ± 1 °C and pH= 7.2 with regard to SCE for every alloy that was tested. The development of corrosion alloys is depicted in Figure 10. The time duration ranged from (0 to 90) minutes, with a 5-minute interval. It is clear from the OCP test that the corrosion potential of the alloys after the addition of Mn became higher and more noble, as shown in Figure (10). This means that the alloy became more noble after the addition of Mn. Figure 11 shows the typical PDT curves of different specimens in Hank's solution at 37 ± 1 °C. The calculated corrosion potentials (Ecorr), corrosion current densities (icorr), and corrosion rate from the polarization curves are summarized in Table 3.

As shown in Table 3, the addition of Mn led to a decrease in corrosion current density. The current density reduces from (35.41 μA/cm^2 for alloy to 12.660 μA/cm^2, 6.903 μA/cm^2 for B1 and B2 alloy, respectively, while the current density reached 9.992 μA/cm^2 for B3 alloy. The biodegradable Zn−1Mg−xMn alloy exhibits lower susceptibility to corrosion compared to the binary Zn-1Mg alloy, indicating that wt.% Mn addition induces significant electrochemically active behavior in the Zn-1Mg alloy, making it less susceptible to corrosion. The CR was significantly reduced after Mn addition to the Zn-1Mg alloy. The corrosion rate for B3 was 0.155 mm/y, while for the base alloy reached 0.769 mm/y. This is a desirable property for biomaterials since it allows for more precise control over the time period over which the material is resorbed by the body. However, the alloy's corrosion potential gradually achieves a more negative value when Mn is added. Although the Ecorr value became more negative after the addition of manganese, the CR decreased significantly. It should be noted that the corrosion resistance improved with increasing Mn content up to 0.3 wt.% Mn, which exhibited the lowest corrosion current density and corrosion rate. However, a slight increase in the corrosion current density and corrosion rate was observed for the 0.4 wt.% Mn alloy (B3), indicating that the optimum Mn content for corrosion resistance was 0.3 wt.%, rather than 0.4 wt.%. This behavior may be attributed to the formation of additional micro-galvanic sites at higher Mn contents.

The improved corrosion resistance observed for the alloys containing 0.2 and 0.3 wt.% Mn could be attributed to the inhibition of the anodic reaction through the formation of protective layers, demonstrating that Mn has a relatively positive effect on the alloy's chemical stability. Furthermore, Mn addition resulted in the formation of a protective passivation film on the alloy in the solution medium. By observing the anodic polarization coefficient (βa) and cathodic polarization coefficient (βc) of the B2 and B3 alloy, it was found that the (βa) value of the

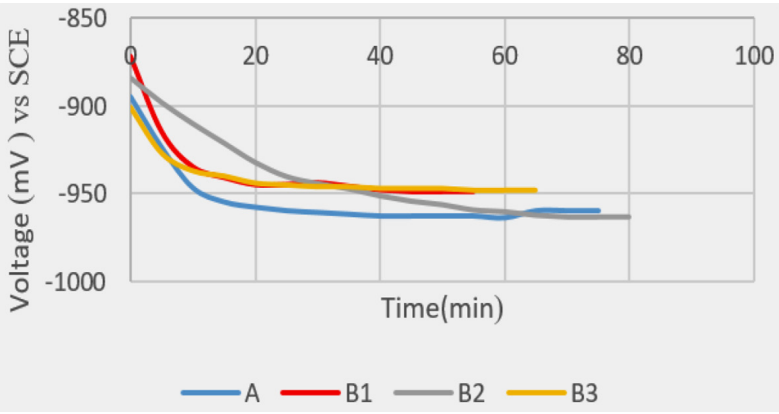


Figure 10. Measurement of OCP of alloys A, B1, B2, and B3 in Hank's solutions

Table 3. The corrosion potential (Ecorr), corrosion current (icorr), and corrosion rate (C.R.) for every alloy in Hank's solution at 37 ± 1 ℃

Sample code	Icorr (μA/cm²)	E(mV)	Corrosion rate (mm/y)	Improvement percentage
A	35.41	-996.1	0.769	-----
B1	12.660	-1026.7	0.194	74.772
B2	6.903	-1014.6	0.099	87.126
B3	9.992	-1057.3	0.155	79.844

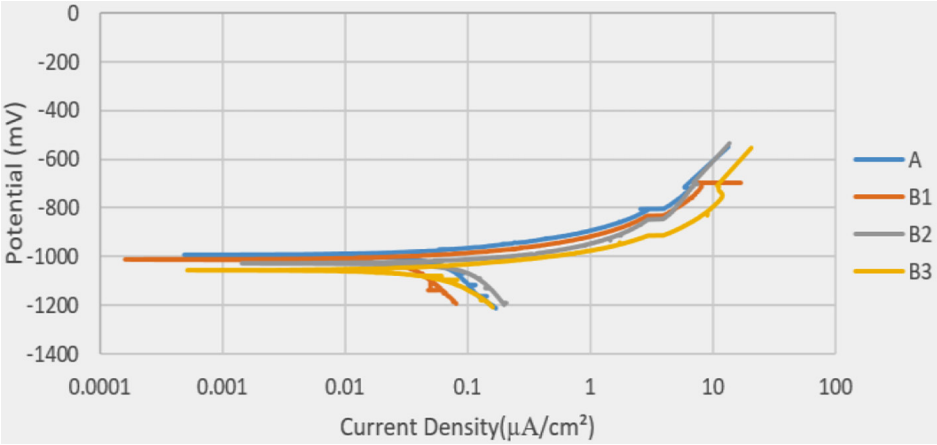


Figure 11. The effect of Mn content on the corrosion rates A, B1, B2, and B3 alloys in Hank's solution at 37±℃

alloys was high while the (βc) value was lower. This suggests that while the cathodic reaction was very quick, the anodic reaction of the alloy decreased during the reaction period. This could be because the cathodic reaction controlled the whole corrosion process, reducing the overall corrosion rate, and the alloy in the solution created a dense passivation coating that successfully regulated the anodic dissolving reaction [11, 20, 31].

Bioactivity

As shown in Figure 12 a and Figure 13 a, the surface morphology of the base alloy after immersion for 7 & 14 days, respectively. It is clear from the figure that hydroxyapatite (HA) growth on the surface was very small, except for a few grains on surface after 14 days of immersion. In turn, Figure 12 b-c and Figure 13 b-c indicate the surface morphology of B1, B3 alloy

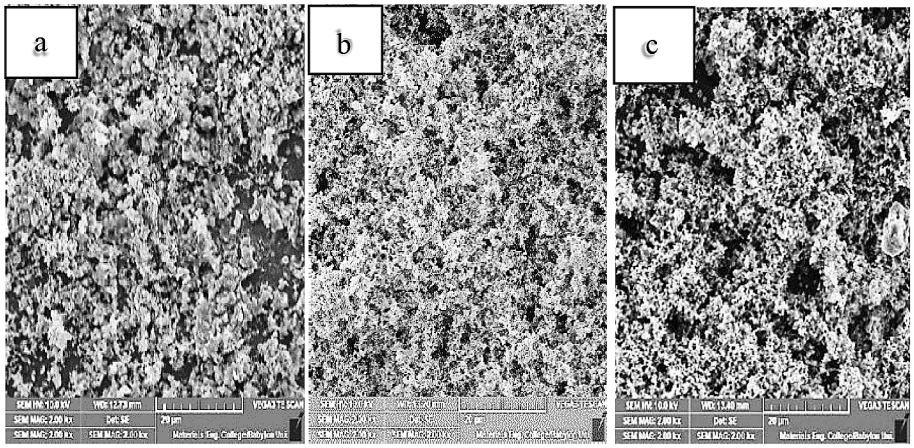


Figure 12. SEM after 7 days immersion in SBF for sample (a) Zn-1Mg, (b) Zn-1Mg+0.2Mn and (c) Zn-1Mg+0.4Mn

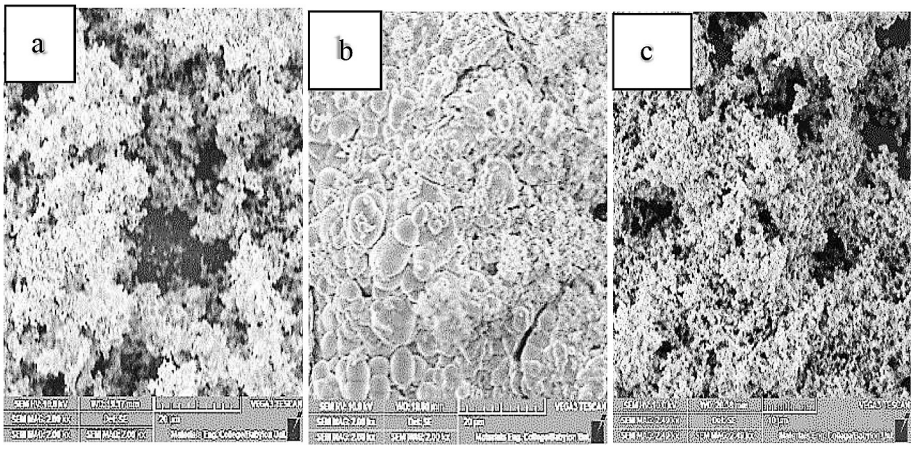


Figure 13. SEM after 14 days immersion in SBF for sample (a) Zn-1Mg, (b) Zn-1Mg+0.2Mn and (c) Zn-1Mg+0.4Mn

after immersion for 7 and 14 days, respectively. The surface morphology of films generated greater amounts of hydroxyapatite on the addition alloys surfaces than on the base alloy surfaces, as presented in SEM images after 7 days, a layer of apatite is formed on the surface, but it is not very dense. It is clear that after 14 days of immersion the surface morphology of films produced with higher concentrations of hydroxyapatite is visible in SEM images. Furthermore, the specimens' surface forms a homogeneous layer that helps biology by improving the capacity of implants inserted inside of humans to fuse with their bones. Furthermore, the formation of a homogeneous calcium phosphate-rich layer indicates good in vitro bioactivity and apatite-forming ability, which may be beneficial for orthopedic applications. As shown in Figures 14, 15 apatite formation in SBF is widely used as *in vitro* indicator for evaluation the bioactivity can be utilized to predict the bioactivity of biomaterials; however, it cannot by itself confirm in vivo bioactivity or osseointegration. In other words, the mentioned phases may improve the formation of the apatite layer on the surface of the B1, B3 sample due to the present of Mn addition to Zn-1Mg alloy. Adding manganese to the Zn–1Mg alloy indirectly enhances bioactivity by

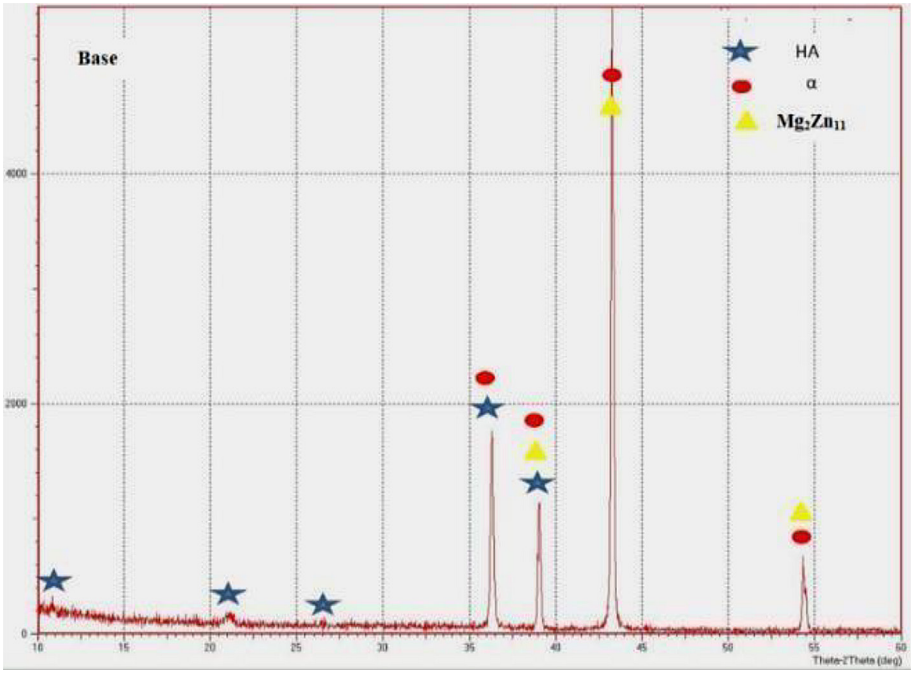


Figure 14. XRD pattern of the sample A (Zn-1Mg) after 14 days of immersion in SBF

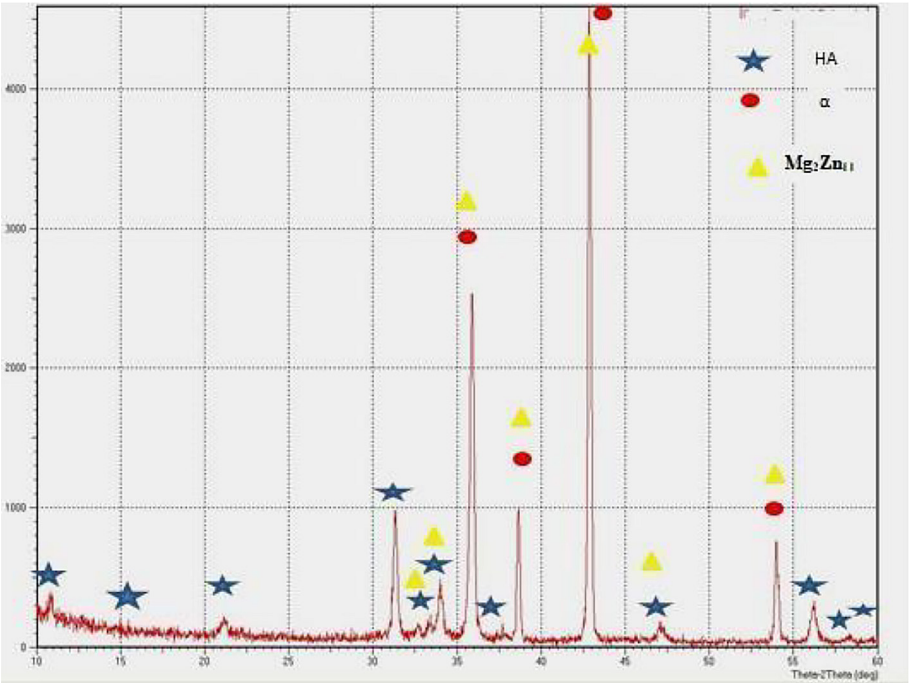


Figure 15. XRD pattern of the sample B3 (Zn-1Mg-0.4Mn) after 14 days of immersion in SBF

refining the grain and improving microstructure homogeneity [20]. Figures 14, 15 show XRD patterns of Zn-1Mg and Zn-1Mg-0.4Mn alloys after 14 days of immersion in SBF respectively. The spectra indicate that the alloys contain (HA) in this study. On the other hand, the base alloys HA peaks are less noticeable than those of other alloys [32, 33]. It can result from the differences in the apatite's location or the formation of a thicker HA layer following manganese addition. In contrast, a number of researchers have shown that this apatite is made up of Ca10(PO4)6(OH)2 that is similar to [34, 35].

Contact angle test

Contact angle is an essential measurement method to measure the wettability of a material's surface [36], which plays a pivotal role in controlling cell adhesion and proliferation, and has

Table 4. Contact angle for Zn-1Mg with and without Mn addition in Hank's solution

No.	Sample	Contact angle value (Deg.)	Contact angle Hank's solution
1	A	95.152	
2	B1	49.886	
3	B2	51.615	
4	B3	40.790	

also been found to be another important aspect in improving the bioactivity of zinc surface. The hydrophobicity or wettability of the Zn-1Mg alloys without and with Mn additions was assessed using the static contact angle "θ" of the droplet on the solid surface, which is a crucial characteristic for quantitatively assessing the wettability of a solid surface. Table 4 clarifies the shape of droplets of solutions on the surface of the base alloy and alloys with Mn additions in Hank's solution. The surface of the base alloy has a higher contact angle of (95.152°) in Hank's solution, which represents a hydrophobic surface compared to the Mn addition sample that presents a contact angle of test values as illustrated in Table 4, all samples containing manganese subjected to the contact angle test exhibit hydrophilic properties [24]. The key to osteoblast growth is the implant's wettability. Numerous studies showed that the surface of biomaterials with good biocompatibility and moderate hydrophilicity may promote cell proliferation [37, 38].

CONCLUSIONS

This study investigated how the addition of Mn affected the mechanical, corrosion, and microstructural properties of Zn-1Mg biodegradable alloys. The following conclusions have been drawn:

1. Powder metallurgy has successfully synthesized ternary Zn-1Mg-xMn (x=0.2, 0.3, and 0.4 wt.%) bio alloys, showing a refined microstructure with α-Zn matrix and second Mg-2Zn11 phases.
2. Due to solid solution grain boundary strengthening mechanisms, the micro hardness increased significantly with the addition of Mn, peaking at 86.21 HV for the 0.4 weight percent Mn alloy.
3. The addition of Mn (0.2, 0.3, and 0.4 wt.%) improved the corrosion resistance compared with the base Zn-1Mg alloy. The best corrosion performance was obtained for the alloy containing
4. 0.3 wt.% Mn, which exhibited the lowest corrosion rate (0.099 mm/y), corresponding to an improvement of 87.126% compared with the base alloy.
5. The addition of Mn promoted calcium phosphate deposition during SBF immersion and significantly reduced the contact angle from 95.152° for the base alloy to 40.790° for the alloy containing 0.4 wt.% Mn, indicating enhanced in vitro apatite-forming ability and surface wettability.
6. The combined improvements in micro hardness, corrosion resistance, wettability, and in vitro bioactivity demonstrate that Mn is an effective alloying element for enhancing the performance of Zn-1Mg biodegradable alloys.

REFERENCES

1. Levy, G. K., Goldman, J., Aghion, E. The prospects of zinc as a structural material for biodegradable implants: A review. Metals, 2017; 7(10), 402. https://doi.org/10.3390/met7100402
2. Balani, K., Verma, V., Agarwal, A., Nara-yan, R. Biosurfaces: A Materials Science and Engineering Perspective. John Wiley & Sons, Hoboken, NJ, 2015.
3. Li, C., et al. Design of biodegradable, implantable devices towards clinical translation. Nature Reviews Materials, 2020; 5(1), 61–81.
4. Krystýnová, M., Doležal, P., Fintová, S., Březina, M., Zapletal, J., Wasserbauer, J. Preparation and characterization of zinc materials prepared by powder metallurgy. Metals, 2017; 7(10), 396. https://doi.org/10.3390/met7100396
5. Sikora -Jasinska, M., Mostaed, E., Mostaed, A., Beanland, R., Mantovani, D., Vedani, M. Fabrication, mechanical properties and in vitro degradation behavior of newly developed ZnAg alloys for degradable implant applications. Materials Science and Engineering: C, 2017; 77, 1170–1181 https://doi.org/10.1016/j.msec.2017.03.326
6. Mostaed, E., Sikora-Jasinska, M., Mostaed, A., Loffredo, S., Demir, A. G., Previtali, B., Mantovani, D., Beanland, R., Vedani, M. Novel Zn-based alloys for biodegradable stent applications: Design, development and in vitro degradation. Journal of the Mechanical Behavior of Biomedical Materials, 2016; 60, 581–602.
7. Yang, H., Jia, B., Zhang, Z., Qu, X., Li, G.,Lin, W., Zhu, D., Dai, K., Zheng, Y. Alloying design of biodegradable zinc as promising bone implants for load-bearing applications. Nature Communications, 2020; 11, 401. https://doi.org/10.1038/s41467-019-14153-7
8. Gu, X., Li, Y., Qi, C., Cai, K. Biode-gradable magnesium phosphates in biomedical applications. Journal of Materials Chemistry B, 2022; 10(12), 2097–2112. https://doi.org/10.1039/D1TB02676K
9. Tayebi, M., Bizari, D., Hassanzade, Z. In-vestigation of mechanical properties and biocorrosion behavior of in situ and ex situ Mg composite for orthopedic implants. Materials Science and Engineering: C, 2020; 113, 110974. https://doi.org/10.1016/j.

msec.2020.110974

10. Zhao, Q., Liu, Z., Zheng, T., Zhang, L., Li, J., Li, X., Cai, Y. Substantial improvement of mechanical properties of Zn–Mg alloys to orthopedic implants via rotary swaging. Scientific Reports, 2025; 15, 29942. https://doi.org/10.1038/s41598-025-29942-x
11. Vida, T., Cruz, C., Barros, A., Cheung, N., Brito, C., Garcia, A. Biodegradable Zn−1wt.%Mg(−0.5wt.%Mn) alloys: Influence of solidification microstructure on their corrosion behavior. Surfaces, 2023; 6(3), 268–280. https://doi.org/10.3390/surfaces6030018
12. Čapek, J., Kubásek, J., Pinc, J., Drahokoupil, J., Čavojský, M., Vojtěch, D. Extrusion of the biodegradable ZnMg0.8Ca0.2 alloy—The influence of extrusion parameters on microstructure and mechanical characteristics. Journal of the Mechanical Behavior of Bio-medical Materials, 2020; 108, 103796. https://doi.org/10.1016/j.jmbbm.2020.103796
13. Yu, L., Tian, Y., Qiao, Y., Liu, X. Mn-containing titanium surface with favorable osteogenic and antimicrobial functions synthesized by PIII&D. Colloids and Surfaces B: Bio interfaces, 2017; 152, 376–384. https://doi.org/10.1016/j.colsurfb.2017.01.037
14. Kong, L., Heydari, Z., Lami, G. H., Saberi, A., Baltatu, M. S., Vizureanu, P. A comprehensive review of the current research status of biodegradable zinc alloys and composites for biomedical applications. Materials, 2023; 16(13), 4797 https://doi.org/10.3390/ma16134797
15. Lu, C., Song, C., Yu, Y., Yang, L., Zheng, W., Luo, F., et al. Biodegradable zinc alloys with high strength and suitable mechanical integrity as bone repair metals. Scientific Re-ports, 2024; 14(1), 30558. https://doi.org/10.1038/s41598-024-81729-4
16. Abdiyan, F., Mahmudi, R., Ghasemi, H.M. Effect of Mn addition on the microstructure, mechanical properties and corrosion resistance of a biodegradable Mg–Gd–Zn alloy. Materials Chemistry and Physics, 2021; 271,124878 https://doi.org/10.1016/j.matchem-phys.2021.124878
17. Ben Tzion-Mottye, L., Ron, T., Eliezer, D., Aghion, E. The effect of Mn on the mechanical properties and in vitro behavior of biodegradable Zn–2%Fe alloy. Metals, 2022; 12(8), 1291. https://doi.org/10.3390/met12081291
18. Kubásek, J., Dvorský, D., Čapek, J., Pinc, J., Vojtěch, D. Zn–Mg biodegradable compo-site: Novel material with tailored mechanical and corrosion properties. Materials, 2019; 12(23), 3930. https://doi.org/10.3390/ma12233930
19. Supardi, A., Willy, S., Hikmawati, D. Syn-thesis and characterization of Zn–Mg alloys as biodegradable materials. Key Engineering Materials, 2020; 860, 205–212. https://doi.org/10.4028/www.scientific.net/KEM.860.205
20. Cheng, X., Lin, Q., Jin, H., Han, F., Dou, X., Zhang, X., et al. Effect of Mn content on the corrosion behavior and biocompatibility of biodegradable Zn-Mn alloys. Scientific Reports, 2025; 15(1), 8958. https://doi.org/10.1038/s41598-025-93584-0
21. Watroba, M., Bednarczyk, W., Kawałko, J., Mech, K., Marciszko, M., Boelter, G., Ban-zhaf, M., Bała, P. Design of novel Zn-Ag-Zr alloy with enhanced strength as a potential biodegradable implant material. Materials & Design, 2019; 183, 108154. https://doi.org/10.1016/j.matdes.2019.108154
22. Al-Khaqani, B. H., Dawood, N. M. Investi-gation of the metallurgical, degradation behavior, and mechanical characteristics of Mg-2Al-1Nd: Novel magnesium alloy. Advances in Science and Technology Research Journal, 2023); 17(5), 302–312. https://doi.org/10.12913/22998624/170974
23. Mollaei, N., Razavi, S. H., Aboutalebi, M. R., Fatemi, S. M. Effect of Mn addition on the microstructure, mechanical, and corrosion properties of an extruded biodegradable Zn-0.2Mg alloy. Journal of Materials Research and Technology, 2023; 22, 1983–1998. https://doi.org/10.1016/j.jmrt.2022.12.145
24. García-Mintegui, C., Córdoba, L. C., Buxa-dera-Palomero, J., Marquina, A., Jiménez-Pi-qué, E., Ginebra, M. P., et al. Zn-Mg and Zn-Cu alloys for stenting applications: From nanoscale mechanical characterization to in vitro degradation and biocompatibility. Bioactive Materials, 2021; 6(12), 4430–4446. https://doi.org/10.1016/j.bioactmat.2021.04.028
25. Hayyawi, A. R., Al-Ethari, H., Haleem, A. H. Surface modification of the Ti-35Nb-7Zr-5Ta bio alloy by the PM-EDM route. Advances in Science and Technology Research Journal, 2024; 18(3), 140–150. https://doi.org/10.12913/22998624/186159
26. Li, J., Han, P., Ji, W., Song, Y., Zhang, S., Chen, Y., Zhao, C., Zhang, F., Zhang, X., Jiang, Y. The in vitro indirect cytotoxicity test and in vivo interface bioactivity evaluation of biodegradable FHA coated Mg–Zn alloys. Materials Science and Engineering: B, 2011; 176(20), 1785–1788. https://doi.org/10.1016/j.mseb.2011.09.009
27. Vojtěch, D., Kubásek, J., Šerák, J., No-vák, P. Mechanical and corrosion properties of newly developed biodegradable Zn-based alloys for bone fixation. Acta Biomaterialia, 2011; 7(9), 3515–3522. https://doi.org/10.1016/j.actbio.2011.05.008
28. Kubásek, J., Vojtěch, D., Jablonská, E., Po-spíšilová, I., Lipov, J., Ruml, T. Structure, mechanical characteristics and in vitro degradation, cytotoxicity, genotoxicity and mutagenicity of novel biodegradable Zn–Mg alloys. Materials Science and Engineering: C, 2016; 58, 24–35 https://doi.org/10.1016/j.msec.2015.08.015
29. Voshage, M., Megahed, S., Schückler, P. G., Wen,

P., Qin, Y., Jauer, L., et al. Additive manufacturing of biodegradable Zn-xMg alloys: Effect of Mg content on manufacturability, microstructure and mechanical properties. Materials Today Communications, 2022; 32, 103805. https://doi.org/10.1016/j.mtcomm.2022.103805

30. Kolawole, M. Y., Aweda, J. O., Iqbal, F., Ali, A., Abdulkareem, S. Mechanical properties of powder metallurgy processed biodegradable Zn-based alloy for biomedical application. Int. J. Mater. Metall. Eng., 2019; 13(12), 558–563.
31. Niinomi, M., Narushima, T., Nakai, M. (Eds.). Advances in Metallic Biomaterials: Tissues, Materials and Biological Reactions (Vol. 3). Springer, Berlin, Heidelberg, 2015. https://doi.org/10.1007/978-3-662-46836-4
32. Kokubo, T., Takadama, H. How useful is SBF in predicting in vivo bone bioactivity? Biomaterials, 2006; 27(15), 2907–2915. https://doi.org/10.1016/j.biomaterials.2006.01.017
33. Topuz, M. Hydroxyapatite–Al2O3 reinforced poly (lactic acid) hybrid coatings on magnesium: Characterization, mechanical and in vitro bioactivity properties. Surfaces and Interfaces, 2023; 37, 102724. https://doi.org/10.1016/j.surfin.2023.102724
34. Sims, A. Fabrication and Corrosion Assess-ment of Biodegradable Metallic Alloys for Pa-tient-Specific Bone Implant Applications (Master's thesis). The University of Tennessee at Chattanooga 2021.
35. Al-Reda, A. K. A., Dawood, N. M., Kareem, S. A. J. Titania coating for biomedical applications on 2205 duplex stainless steel substrate using the sol gel technique. AIP Conference Proceedings, 2025; 3303(1), 070007. https://doi.org/10.1063/5.0256216
36. Erbil, H. Y. The debate on the dependence of apparent contact angles on drop contact area or three-phase contact line: A review. Surface Science Reports, 2014; 69(4), 325–365. https://doi.org/10.1016/j.surfrep.2014.06.001
37. Shi, Y., Yang, L., Wang, L., Zhang, Q., Zhu, X., Sun, W., et al. Corrosion and biocompatibility of pure Zn with a micro-arc-oxidized layer coated with calcium phosphate. Coat-ings, 2021; 11(11), 1425. https://doi.org/10.3390/coat-ings11111425
38. Abd Al-Reda, A. K., Dawood, N. M., Kareem, S. J. Modification of 2205 duplex stainless steel properties through solution heat treatment and surface enhancement with sol-gel coatings for biomedical applications. Journal of Ceramic Processing Research, 2024; 25(3), 365–374. https://doi.org/10.36410/jcpr.2024.25.3.365